

Accurate Lungs Segmentation on CT Chest Images by Adaptive Appearance-Guided Shape Modeling

Ahmed Soliman, *Member, IEEE*, Fahmi Khalifa, *Member, IEEE*, Ahmed Elnakib, *Member, IEEE*, Mohamed Abou El-Ghar, Neal Dunlap, Brian Wang, Georgy Gimel'farb, Robert Keynton, and Ayman El-Baz*, *Senior Member, IEEE*

Abstract—To accurately segment pathological and healthy lungs for reliable computer-aided disease diagnostics, a stack of chest CT scans is modeled as a sample of a spatially inhomogeneous joint 3D Markov-Gibbs random field (MGRF) of voxel-wise lung and chest CT image signals (intensities). The proposed learnable MGRF integrates two visual appearance sub-models with an adaptive lung shape submodel. The first-order appearance submodel accounts for both the original CT image and its Gaussian scale space (GSS) filtered version to specify local and global signal properties, respectively. Each empirical marginal probability distribution of signals is closely approximated with a linear combination of discrete Gaussians (LCDG), containing two positive dominant and multiple sign-alternate subordinate DGs. The approximation is separated into two LCDGs to describe individually the lungs and their background, i.e., all other chest tissues. The second-order appearance submodel quantifies conditional pairwise intensity dependencies in the nearest voxel 26-neighborhood in both the original and GSS-filtered images. The shape submodel is built for a set of training data and is adapted during segmentation using both the lung and chest appearances. The accuracy of the proposed segmentation framework is quantitatively assessed using two public databases (ISBI VESSEL12 challenge and MICCAI LOLA11 challenge) and our own database with, respectively, 20, 55, and 30 CT images of various lung pathologies acquired with different scanners and protocols. Quantitative assessment of our framework in terms of Dice similarity coefficients, 95-percentile bidirectional Hausdorff distances, and percentage volume differences confirms the high accuracy of our model on both our database ($98.4 \pm 1.0\%$, 2.2 ± 1.0 mm, $0.42 \pm 0.10\%$) and the VESSEL12 database ($99.0 \pm 0.5\%$, 2.1 ± 1.6 mm, $0.39 \pm 0.20\%$), respectively. Similarly, the accuracy of our approach is further verified via a blind evaluation by the organizers of

Manuscript received June 17, 2016; revised August 26, 2016; accepted August 29, 2016. Date of publication September 12, 2016; date of current version December 29, 2016. Asterisk indicates corresponding author.

A. Soliman, F. Khalifa, and A. Elnakib are with the Biolmaging Laboratory, Bioengineering Department, University of Louisville, Louisville, KY 40292 USA.

M. A. El-Ghar is with the Radiology Department, Urology and Nephrology Center, University of Mansoura, Mansoura 35516, Egypt.

N. Dunlap and B. Wang are with the Radiation Oncology Department, University of Louisville, Louisville, KY 40202 USA.

G. Gimel'farb is with the Department of Computer Science, University of Auckland, Auckland 1142, New Zealand.

R. Keynton is with the Bioengineering Department, University of Louisville, Louisville, KY 40292 USA.

*A. El-Baz is with the Biolmaging Laboratory, Bioengineering Department, University of Louisville, Louisville, KY 40292 USA (e-mail: aselba01@louisville.edu).

Digital Object Identifier 10.1109/TMI.2016.2606370

the LOLA11 competition, where an average overlap of 98.0% with the expert's segmentation is yielded on all 55 subjects with our framework being ranked first among all the state-of-the-art techniques compared.

Index Terms—Adaptive shape model, computed tomography, lung segmentation, Markov-Gibbs random field.

I. INTRODUCTION

AUTOMATED lung segmentation on chest CT scans is crucial for efficient computer-aided diagnosis (CAD) of pulmonary diseases, such as, lung cancer. Unfortunately, the large variety of images and diagnostic measurements for different lung pathologies make accurate, fast, and low-cost segmentation a challenge. For instance, pathology-related segmentation failures lose important data, being needed for studying radiation pneumonitis development [1]. As shown by Armato et al. [2] the accuracy of lung segmentation can affect lung nodules detection by 17%.

In the application to CT chest images, most of the earlier segmentation techniques [3]–[9] presume only the lungs are darker than the other chest tissues, which might result in failure to detect nodules in the case of severe lung pathologies. To avoid such failures, more recent lung segmentation methods, which are briefly reviewed below, consider visual appearances [10], [11], shapes [12]–[17], or hybrid techniques [18]–[22] to account for normal and pathological tissues. A more detailed survey of current lung segmentation techniques can be found in [23].

Appearance-based segmentation employs texture information to distinguish between objects where the edges are not defined by clear boundaries. Wang et al. [11] used classical Haralick's texture descriptors to discriminate, on chest CT scans, between normal and pathological tissues with unclear boundaries for moderate or severe interstage lung disease (ILD). The descriptors, including energy, entropy, contrast, maximum probability, and inverse difference moment, characterize the local gray-level co-occurrence matrices. First, normal tissues and moderate ILD parenchyma were segmented by simple thresholding of the voxel-wise signals. Then, the abnormal regions with severe ILD, which depict the local descriptors, were found on the appearance images, and combined with the initially segmented regions. This method demonstrated an average overlap of 96.7% with the “gold standard” manual method on a test database of

76 CT scans (31 normal and 45 abnormal lungs). In another study, Korfiatis et al. [18] segmented lung data, including cases with interstitial pneumonia, first by using voxel-wise gray levels only. Subsequently the initial segmentation was refined by classifying the voxels by a support vector machine classifier to account for statistics of both the gray levels and wavelet coefficients, whereas Lassen et al. [19] used a sequence of morphological operations to refine the initial threshold-based segmentation of the pulmonary airspaces. Kockelkorn et al. [21] segmented the lungs with a k -nearest-neighbor classifier, trained on available prior data; however, to account for severe abnormalities, the user had to interactively correct the initial classification.

Shape-based segmentation exploits specific lung shape priors with some variability among the scans to yield more accurate segmentation. Sun et al. [15] matched a 3D active shape model to a CT chest scan to roughly define the initial lung borders and then refined the segmented lungs with a global surface optimization method developed by Li et al. [24]. Van Rikxoort et al. [16] segmented the lungs using region growing and morphological operations methods, then automatically performed a multi-atlas-based refinement if a pathology-related segmentation error was detected automatically due to a statistical deviation from a predefined range of lung volume and shape measurements. Sluimer et al. [14] used 15 chest CT scans to build a probabilistic atlas of normal lung fields and registered a pathological lung scan to the atlas in order to segment the lungs with severe pathologies. To segment pathological lungs, Sofka et al. [25] used a set of anatomical landmarks on the ribs and spine to initialize the shape model and then refined the model by iterative surface deformation. Similarly, an atlas-based segmentation model in combination with a deformable model was applied by Zhou et al. [13] to segment lungs with large tumors; whereas, Nakagomi et al. [17] implemented a graph-cut segmentation technique, that incorporated shape and other prior information about neighboring lung structures, on pathological lung images including pleural effusion.

Hybrid segmentation combines various segmentation techniques to reach higher accuracies. Birkbeck et al. [20] added statistical learning to anatomical constraints derived from neighboring anatomical structures (heart, liver, spleen, and ribs), to segment lungs. These structures were first detected by statistical classifiers and then used as geometrical constraints for deforming the lung mesh. Mansoor et al. [10] segmented pathological lungs with a wide range of abnormalities in two steps. Initially, the lung parenchyma was segmented on the basis of fuzzy connectedness [26], and the differences between the rib-cage and lung parenchyma volumes were analyzed to determine the pathology. Subsequently, the segmentation was refined, by applying texture descriptors, to identify the pathological tissues that might have been missed during the initial segmentation procedure. Kockelkorn et al. [12] divided the chest CT scan into 3D volumes-of-interest (VOIs) with voxels of similar intensities and classified each VOI as either the lung or background. Then, the misclassified voxels were corrected either interactively or using a slice-wise supervised classification technique. Hua et al. [22] segmented the lungs

by optimizing a graph-supported cost function of voxel-wise intensities and their spatial gradients, taking into account the boundary smoothness and rib constraints.

However, the above methods for automated or semi-automated segmentation of normal and pathological lungs from CT chest images have several drawbacks. Specifically, some of the methods rely on expensive and user-dependent interactions with a radiologist, or depend on anatomical landmarks, which are difficult to determine, especially when pathological tissues are present. Furthermore, when a pathology detector is employed, the overall accuracy considerably decreases after the detection fails. In addition, active appearance models make segmentation too sensitive to model initialization and number of control points. Moreover, most of the methods were designed for a specific type of lung pathology, e.g., nodules, and thus may fail on other types of pathological tissues. To partially overcome these drawbacks, we propose a novel framework, being capable to segment with a high level of accuracy both normal and pathological lungs from chest CT images acquired via various scanners and protocols. Due to integrating an adaptive shape prior with easy-to-learn first-order visual appearance models and a 2nd-order 3D MGPF-based model of spatial voxel interactions, the framework is applicable to a wide variety of pathologies, including tumors, pulmonary sarcoidosis, pleural effusion, consolidation, fibrosis, and cavities. To the best of our knowledge, we are the first to introduce a probabilistic map accounting for not only region labels, but also intensities in neighboring spatial voxel locations as an adaptive shape prior. The framework, detailed in Section II, was extensively validated on three databases (Section III) and ranked first by the third-party evaluation of LOLA11 challenge.

II. METHODS

All 3D CT chest scans are initially pre-processed to identify their background voxels, (air and bed), by region growing and analyzing connected components. Because detailed prior information about lung shapes significantly improves the segmentation accuracy, our framework (Fig. 1) builds a spatially-variant shape prior from a pre-selected training database of 3D CT scans of normal and pathological lungs. The training scans are accurately co-aligned using a B-spline-based nonrigid registration [27], detailed in Section II-A. Unlike more conventional alternatives, the proposed shape prior is adapted to a given input, or test CT scan. The latter is similarly aligned to the training database and a 3D deformation field of aligning voxel-to-voxel translations is stored in order to guide the process of building the shape prior.

The framework analyzes both the original input and its Gaussian scale-space (GSS) versions, being formed by convolving with 3D moving Gaussian kernels [28] (Section II-B). The GSS smoothing adds longer-range properties to original voxel-wise intensities and their pairwise co-occurrences in the nearest 26-neighborhoods of each voxel. For segmenting the input image, first- and second-order lungs-background models are learned and combined with the shape priors separately for the input image and each of its GSS versions. The first-order models are built by accurate LCDG-based

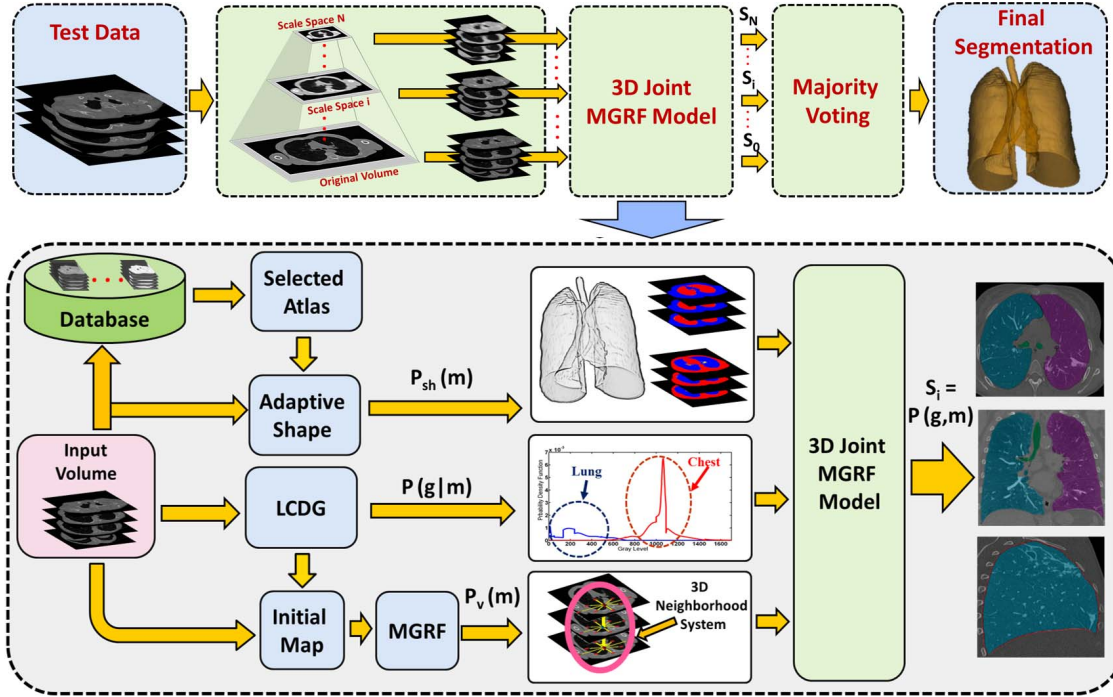


Fig. 1. Our framework for segmenting lungs from chest CT images.

approximations of empirical marginal probability distributions of intensities over the whole image and estimations of individual marginal distributions of the lung and background intensities [29] (Section II-C). The 2nd-order spatially uniform MGRF models with multiple pairwise interactions of the nearest-neighbor region labels [30] are learned to describe initial lungs-background region maps (Section II-D).

The input image, as well as each of its smoothed GSS versions, is separately segmented by combining their learned probabilistic first- and 2nd-order models together with the adaptive shape priors into a joint MGRF model of images and their region maps (Section II-E). Finally, a majority rule is used to merge the resulting separate segmentations into a final lung-background region map (Section II-F).

Basic notation: Let $\mathbf{Q} = \{0, 1, \dots, Q-1\}$ and $\mathbf{K} = \{0, 1\}$ be a finite set of integer gray levels and region labels (background chest tissues—“0”, and lung tissues—“1”), respectively. Let $\mathbf{r} = (x, y, z)$ be a voxel in integer 3D (x, y, z) -coordinates spanning from $(0, 0, 0)$ to (X, Y, Z) . Let a finite 3D arithmetic lattice $\mathbf{R} = \{\mathbf{r} = (x, y, z) : 0 \leq x \leq X, 0 \leq y \leq Y, 0 \leq z \leq Z\}$ support the grayscale CT images, $\mathbf{g} = \{g_{\mathbf{r}} : \mathbf{r} \in \mathbf{R}; g_{\mathbf{r}} \in \mathbf{Q}\}$, and their region, or segmentation maps, $\mathbf{m} = \{m_{\mathbf{r}} : \mathbf{r} \in \mathbf{R}; m_{\mathbf{r}} \in \mathbf{K}\}$.

A. Adaptive Probabilistic Shape Prior

The proposed appearance-guided adaptive shape prior is built from a pre-selected and manually segmented training database of 3D chest CT scans. To reduce variations and maximize overlaps between the lungs for estimating the prior, each source volume f (i.e., each of the database subjects) is aligned to the target volume, or reference template g on a domain $\Omega \subset \mathbb{R}^3$ by using a non-rigid registration. Given a certain source f , the registration estimates the deformation

field \mathcal{T} for all $x \in \Omega$, by displacing a sparse grid, $\Omega' \subset \Omega$; ($|\Omega'| \ll |\Omega|$), of control points, ξ :

$$\mathcal{T}(x) = x + \sum_{\xi \in \Omega'} \zeta(\|x - \xi\|) \Delta_{\xi} \quad (1)$$

where Δ_{ξ} is the displacement vector of the control point ξ and the weighting function $\zeta(\cdot)$ measures the contribution of any control point in Ω' to the displacement of a point in Ω . The goal deformation field minimizes the point-wise dissimilarity between the target g and the deformed source f :

$$E(\mathcal{T}) = \frac{1}{|\Omega'|} \sum_{\xi \in \Omega'} \int_{\Omega} \frac{\phi(g(x), f(\mathcal{T}(x)))}{\zeta(\|x - \xi\|)} dx \quad (2)$$

where ϕ is the dissimilarity function (we used the sum of absolute differences). The objective function in Eq. (2) is minimized using a Markov random field model of displacements of the control points ξ [31]. The dense displacement field is then determined from the control point displacements through representing free form deformations (FFDs) via cubic B-splines. We have selected this method because it is fully automated (no manual initialization or hand-picked landmarks) and has low computational time. More details can be found in [27], [31], [32].

To handle both the normal and pathological lungs, our database, $\mathbf{S} = \{s_i = (g_i, m_i) : i = 1, 2, \dots, N\}$, contains 3D scans of different normal and pathological lungs, having been chosen to represent typical inter-subject variations, and their true region maps. The database subjects are selected using the principal component analysis (PCA). The PCA calculates principal components (PCs) of the covariance matrix between all the available subjects from the database (50 subjects in our work). Then, instead of defining a new template domain

for the top N PCs, the original N subjects with the highest-magnitude coefficients of each of the top N PCs are selected to approximate projections computed by the PCA [33] for each test image. In our experiments below, the $N = 20$ training images, having been selected from our locally acquired database of 50 subjects, had different sizes, data spacing, and slice thickness, which ranged from $512 \times 512 \times 270$ to $512 \times 512 \times 450$; 0.703 to 1.37 mm, and 0.703 to 2.50 mm, respectively. **Selected cross sections from each of the 20 subjects can be found in the supplementary materials, available in the supplementary files /multimedia tab.** Co-aligning these images with the reference template overcomes their variations and makes their size and resolution identical. Because every training image has its own deformation field that maps its voxels to the reference template, accurate mappings between the template and training images are guaranteed.

A test 3D CT image \mathbf{t} to be segmented is co-aligned with the training database using the same template and B-spline-based nonrigid registration [27]. Then its customized atlas is extracted by computing conventional normalized cross correlations (NCC) of Eq. (3) between the chest region in the aligned test image \mathbf{t} and the chest region in each database image, $\mathbf{g}_{l:i}$, to select the top J similar lungs.

$$NCC_{\mathbf{t},\mathbf{g}_i} = \frac{\sum_{\mathbf{r} \in \mathbf{R}} (\mathbf{t}_{\mathbf{r}} - \mu_{\mathbf{t}})(\mathbf{g}_{i:\mathbf{r}} - \mu_{\mathbf{g}_{l:i}})}{\sqrt{\sum_{\mathbf{r} \in \mathbf{R}} (\mathbf{t}_{\mathbf{r}} - \mu_{\mathbf{t}})^2} \sqrt{\sum_{\mathbf{r} \in \mathbf{R}} (\mathbf{g}_{i:\mathbf{r}} - \mu_{\mathbf{g}_{l:i}})^2}} \quad (3)$$

where $\mu_{\mathbf{t}}$ and $\mu_{\mathbf{g}_{l:i}}$ are the average intensities for \mathbf{t} and $\mathbf{g}_{l:i}$.

Visual appearances of the test and training images guide the shape prior adaptation as follows (this process is also outlined in Algorithm 1 summarizing the proposed segmentation framework). Each voxel \mathbf{r} of the test image \mathbf{t} is mapped to the database lattice by the deformation field aligning \mathbf{t} to the database. A subject-specific atlas is built from the top J ; $J \leq N$, training images \mathbf{g}_i selected in accord with their correlations $NCC_{\mathbf{t},\mathbf{g}_i}$ of Eq. (3) ($J = 15$ in our experiments below). To adapt the shape prior at each mapped location \mathbf{r} , an initial search cube $\mathbf{C}_{\mathbf{r}}$ of size $n_{x:i} \times n_{y:i} \times n_{z:i}$ is centered at the mapped location \mathbf{r} for finding in the cube all the atlas voxels with signal deviations to within a predefined fixed range, τ , from the mapped input signal, $t_{\mathbf{r}}$. If such voxels are absent in the atlas, the cube size increases iteratively until the voxels within the predefined signal deviation range are found or the final cube size is reached ($n_{x:i} = n_{y:i} = n_{z:i} = 3$; τ from 50 to 125 with the step of $\Delta\tau = 25$, and the final cube size of $n_{x:f} = n_{y:f} = n_{z:f} = 11$ were used in our experiments). Then the voxel-wise probabilities, $P_{sh:\mathbf{r}}(k)$; $k \in \mathbf{K}$, for the adaptive shape prior $P_{sh}(\mathbf{m}) = \prod_{\mathbf{r} \in \mathbf{R}} P_{sh:\mathbf{r}}(m_{\mathbf{r}})$ are estimated based on the found voxels of similar appearance and their labels. Let $\mathbf{v}_{j:\mathbf{r}} = \{\rho : \rho \in \mathbf{R}; \rho \in \mathbf{C}_{\mathbf{r}}; |g_{j:\rho} - t_{\mathbf{r}}| \leq \tau\}$ be a subset of similar voxels within the cube $\mathbf{C}_{\mathbf{r}}$ in the training image \mathbf{g}_j . Let $v_{j:\mathbf{r}} = \text{card}(\mathbf{v}_{j:\mathbf{r}})$ denote the cardinality (number of voxels) of this subset; $v_{\mathbf{r}} = \sum_{j=1}^J v_{j:\mathbf{r}}$, and $\delta(z)$ be the Kronecker's delta-function: $\delta(0) = 1$ and 0 otherwise. Then

$$P_{sh:\mathbf{r}}(k) = \frac{1}{v_{\mathbf{r}}} \sum_{j=1}^J \sum_{\rho \in \mathbf{v}_{j:\mathbf{r}}} \delta(k - m_{j:\rho}) \quad (4)$$

Algorithm 1 Proposed Lung Segmentation Framework

- **Input:** Read a given test 3D CT image and form its smoothed GSS versions.
 - Appearance-guided estimation of the adaptive shape priors:
 1. Align the test image to the training database and obtain its voxel-wise deformation field.
 2. Construct the subject-specific atlas of the J top training images by their cross-correlation with the test image.
 3. Estimate the appearance-guided adaptive shape prior $P_{sh}(\mathbf{m})$ separately for the original and GSS-smoothed test images by calculating the voxel-wise empirical probabilities of the relevant training lungs-background labels:
 - (a) Map each test voxel to the atlas lattice using the found deformation field.
 - (b) Center the initial $n_{x:i} \times n_{y:i} \times n_{z:i}$ search cube at the mapped voxel.
 - (c) Find within the search cube all the atlas voxels, being close to the test voxel-wise intensity (Hounsfield value) to within a predefined range of $\pm\tau$.
 - (d) If no such voxels are found, increase the search cube iteratively and repeat Steps 3b–3c until the relevant voxels are found or a predefined maximum cube size is reached.
 - (e) If no such voxels are found, increase iteratively the tolerance τ by $\Delta\tau$ and repeat Steps 3b–3d until such voxels are found.
 - (f) Compute the empirical voxel-wise label probabilities based on relative occurrences of each label over all the found relevant voxels.
 4. Segment the lungs individually on the original and GSS-smoothed images:
 - 1) Find an initial region map \mathbf{m} by the voxel-wise Bayesian maximum a posteriori classification of the test image using its estimated shape prior.
 - 2) Identify the conditional appearance (intensity) model $P(\mathbf{g}|\mathbf{m})$ by approximating with the LCDGs, the marginal probability distributions of signals associated with one of the two dominant modes of the mixed empirical marginal for the whole test image.
 - 3) Use the initial region map, \mathbf{m} , to identify the second-order MGFR model, $P_V(\mathbf{m})$, of spatially invariant maps.
 - 4) Perform the final Bayesian segmentation of the lungs using the joint MGFR model of Eq. (10).
 5. **Output:** The final lungs segmentation by combining individually segmented original and GSS-smoothed images with the majority voting.
-

B. Gaussian Scale Space (GSS) Smoothing

This operation $\mathbf{g}_{\sigma} = \mathbf{g} * \mathbf{h}_{\sigma}$ convolves a 3D CT image \mathbf{g} with a 3D Gaussian kernel $\mathbf{h}_{\sigma;\mathbf{c}} = (h_{\sigma;\mathbf{r}-\mathbf{c}} : (\mathbf{r}, \mathbf{c}) \in \mathbf{R}^2)$ [28]:

$$h_{\sigma;\mathbf{r}-\mathbf{c}} = \frac{1}{(2\pi)^{1.5}\sigma^3} \exp\left(-\frac{1}{2\sigma^2}|\mathbf{r} - \mathbf{c}|^2\right) \quad (5)$$

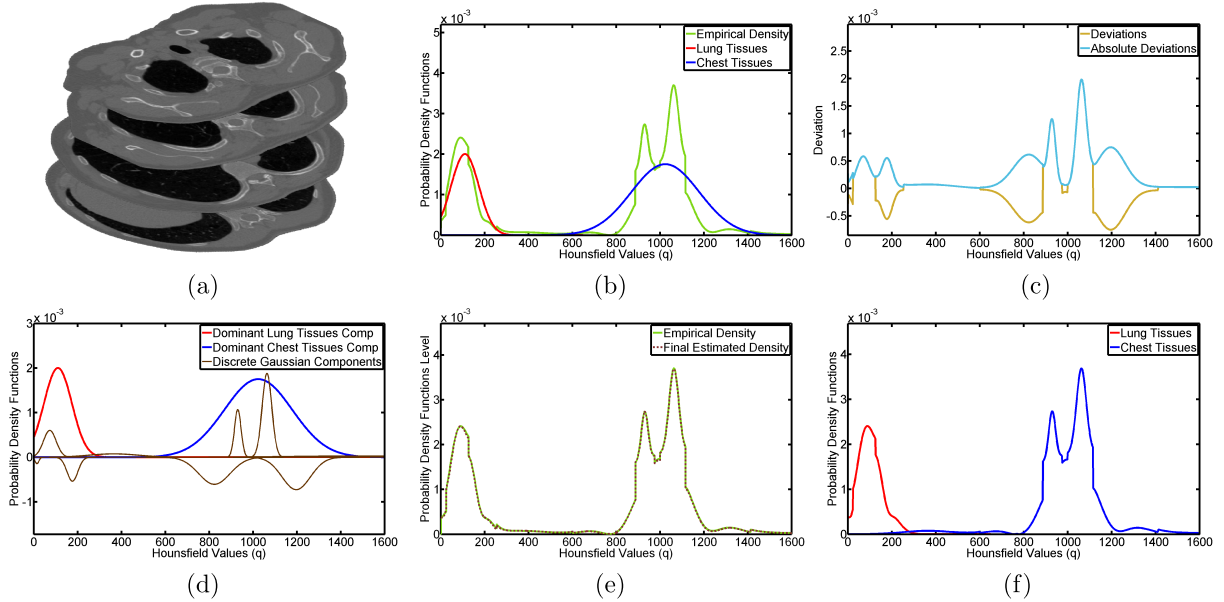


Fig. 2. Typical 3D CT data (a) and its marginal intensity approximated using only two dominant DGs (b); the deviation between the empirical and estimated marginals (c); the dominant and subordinate DGs (d); the final estimated LCDG (e), and the final conditional LCDG models of lung and chest intensities (f).

where $|\mathbf{r} - \mathbf{c}| = \sqrt{(x - x_c)^2 + (y - y_c)^2 + (z - z_c)^2}$ denotes the Cartesian voxel-to-voxel distance and $\mathbf{c} = (x_c, y_c, z_c)$ is the kernel's center. The GSS smoothing reduces signal noise affecting some chest CT scans, integrates longer-range properties of the scans in each voxel-wise signal, and excludes some distortions that may be caused by pathologies. Because it flattens the original image, i.e., decreases the maximal and increases the minimal intensities, only two versions smoothed with the kernels $9 \times 9 \times 5$; $\sigma^2 = 4.5$, and $17 \times 17 \times 5$; $\sigma^2 = 8.5$; were used in our experiments below to extend the overall description of the CT image without losing too many details and affecting the segmentation accuracy.

C. First-Order Appearance (Intensity) Modeling

To accurately separate and approximate conditional marginal probability distributions of intensities (Hounsfield units) for the lungs and surrounding chest tissues, the CT image is modeled as a simple independent random field (IRF) with the same mixed distribution of intensities at each voxel. The mixed empirical distribution of the voxel-wise intensities over the whole image is approximated with an LCDG with two dominant positive DGs and multiple sign-alternate (positive and negative) subordinate DGs. The number of the subordinate DGs and parameters (means and variances) of all the DGs are estimated with the classical Expectation-Maximization (EM) algorithm and its modification accounting for the alternate signs of the DGs [34]. Then the obtained LCDG is separated into conditional lung and chest intensity models for defining the conditional IRF of image signals, given a region map:

$$P(\mathbf{g}|\mathbf{m}) = \prod_{\mathbf{r} \in \mathbf{R}} p_{m_r}(g_r) \quad (6)$$

Basic steps of estimating the conditional lung and chest LCDG models, $P_k = (p_k(q) : q \in \mathbf{Q})$; $k \in \mathbf{K} = \{0, 1\}$, are illustrated in Fig. 2, and Fig. 3 shows a 3D CT image; its GSS-version for

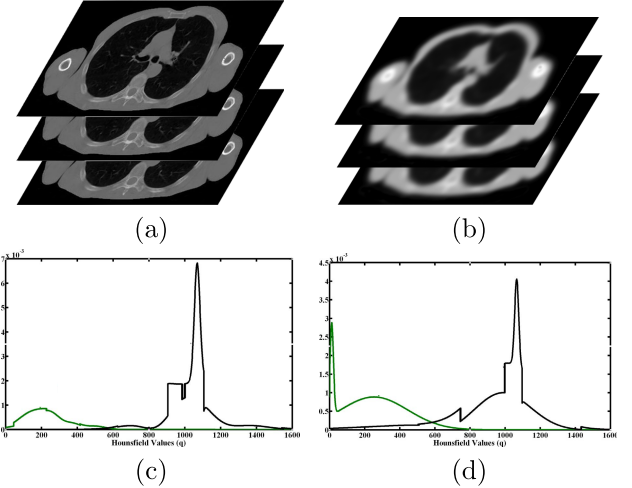


Fig. 3. 3D CT image (a) and its GSS-filtered version (b) for the $33 \times 33 \times 5$ kernel, with the final estimated conditional LCDG models for chest and lung marginals (c,d).

the $33 \times 33 \times 5$ kernel, and the corresponding final estimated conditional LCDG models for chest and lung marginals.

D. Modeling Pairwise Spatial Interactions of Lung Labels

To account for lungs inhomogeneities that may affect the initial Bayesian segmentation, spatial dependencies between the lung voxels are modeled with a spatially invariant second-order MGPF [29], [30] with the nearest voxel 26-neighborhood. This modeling enhances the initial segmentation by calculating the likelihood of each voxel to be lung or non-lung on the basis of the initial labeling of the adjacent voxels. By symmetry considerations, the dependencies are uniform, i.e., independent of orientations in the lattice. Let $\mathbf{V}_a = \{V_a(k, k') = V_{a,eq}\}$. if $k = k'$ and $V_a(k, k') = V_{a,ne}$ if $k \neq k'$: $k, k' \in \mathbf{K}\}$ denote bi-valued Gibbs potentials describing three types of symmetric pairwise dependencies between the labels: $a \in \mathbf{A} = \{\text{hvdc}, \text{hvdu}, \text{hvdl}\}$ where hvdc, hvdu, and hvdl

indicate the horizontal-vertical-diagonal dependencies between each voxel and its closest 26-neighbors in the current (c), upper (u), and lower (l) CT slices, respectively, specified by the subsets of inter-voxel coordinate offsets: $\mathbf{N}_{\text{hvdc}} = \{(\pm 1, 0, 0), (0, \pm 1, 0)\}$, $\mathbf{N}_{\text{hvdu}} = \{(0, 0, 1), (\pm 1, \pm 1, 1)\}$, and $\mathbf{N}_{\text{hndl}} = \{(0, 0, -1), (\pm 1, \pm 1, -1)\}$. Then the Gibbs probability distribution of region maps is proportional to:

$$P_{\mathbf{V}}(\mathbf{m}) \propto \exp \left(\sum_{\mathbf{r} \in \mathbf{R}} \sum_{a \in \mathbf{A}} \sum_{\mathbf{v} \in \mathbf{N}_a} V_a(m_{\mathbf{r}}, m_{\mathbf{r}+\mathbf{v}}) \right) \quad (7)$$

This MGRF is identified by using the approximate analytical maximum likelihood estimates of the potentials [29], [30]:

$$V_{a,\text{eq}} = \frac{K^2}{K-1} \left(f_{\text{eq}:a}(\mathbf{m}) - \frac{1}{K} \right) = 4f_{\text{eq}:a}(\mathbf{m}) - 2 \quad (8)$$

$$V_{a,\text{ne}} = \frac{K^2}{K-1} \left(f_{\text{ne}:a}(\mathbf{m}) - 1 + \frac{1}{K} \right) = 4f_{\text{ne}:a}(\mathbf{m}) - 2$$

where $f_{\text{eq}:a}(\mathbf{m})$ and $f_{\text{ne}:a}(\mathbf{m})$ are empirical probabilities of the equal and non-equal labels pairs, respectively, in all the equivalent voxel pairs $\{(\mathbf{r}, \mathbf{r} + \mathbf{v}) : \mathbf{v} \in \mathbf{N}_a; \mathbf{r} \in \mathbf{R}\}$.

E. Joint MGRF Model of 3D Chest CT Images

To initially segment the lungs, the above unconditional adaptive shape prior, $P_{\text{sh}}(\mathbf{m})$, conditional first-order appearance model, $P(\mathbf{g}|\mathbf{m})$, and unconditional second-order model, $P_{\mathbf{V}}(\mathbf{m})$ of spatial dependencies between the lung labels in Eqs. (7) and (8) are integrated into a joint MGRF model of either original, or GSS-smoothed images, \mathbf{g} , and their region maps, \mathbf{m} :

$$P(\mathbf{g}, \mathbf{m}) = P(\mathbf{g}|\mathbf{m}) \underbrace{P_{\text{sh}}(\mathbf{m}) P_{\mathbf{V}}(\mathbf{m})}_{P(\mathbf{m})} \quad (9)$$

Both the images and region maps are co-aligned to the subject-specific atlas defining the shape prior. The Bayesian maximum a posteriori estimate, $\mathbf{m}^* = \arg \max_{\mathbf{m}} L(\mathbf{g}, \mathbf{m})$, of the region map, given an image \mathbf{g} , maximizes the log-likelihood

$$L(\mathbf{g}, \mathbf{m}) = \log P(\mathbf{g}|\mathbf{m}) + \log P_{\text{sh}}(\mathbf{m}) + \log P_{\mathbf{V}}(\mathbf{m}) \quad (10)$$

F. Classification Using Majority Voting

The majority voting, which is popular in fusing concurrent decisions, is a special case of the weighted voting. Our final segmentation map, $\hat{\mathbf{m}}$, combines by the majority voting the individual Bayesian region maps \mathbf{m} and \mathbf{m}_l , having been built separately for the original image, \mathbf{t} , and its L GSS-transformed versions, $\mathbf{t}_{l:\sigma_l}; l = 1, \dots, L$:

$$\hat{\mathbf{m}}_{\mathbf{r}} = \arg \max_{k \in \{0,1\}} \left\{ \delta(k - m_{\mathbf{r}}) + \sum_{l=1}^L \delta(k - m_{l:\mathbf{r}}) \right\} \quad (11)$$

The two GSS kernels: $l = 1, 9 \times 9 \times 5; \sigma_1^2 = 4.5$, and $l = 2, 17 \times 17 \times 5, \sigma_2^2 = 8.5$ —were used in our experiments below.

The main algorithmic components of our framework are detailed in Appendix I and Figs. 14 – 21

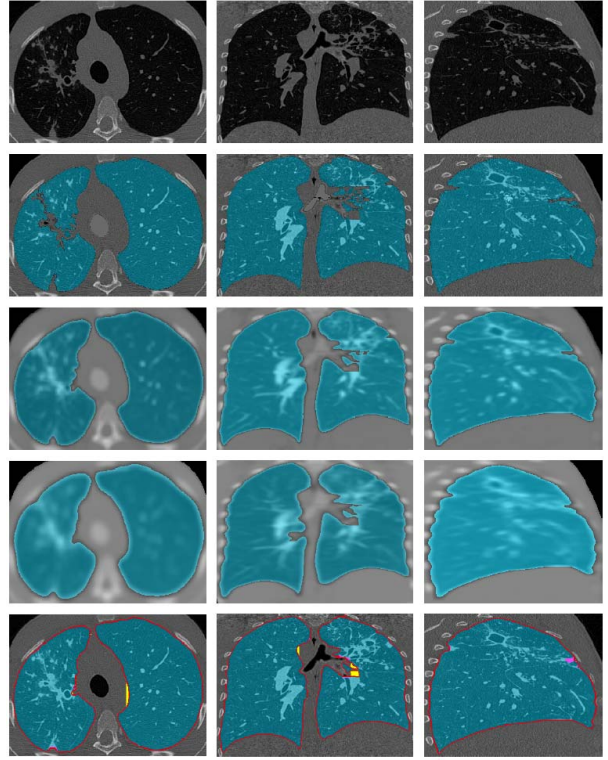


Fig. 4. 3D lung segmentation (the UoLDB): 2D axial (first column), coronal (second column) and sagittal (third column) cross-sections of an original image (first row); its segmentation (second row); segmentation of the GSS-filtered images with $9 \times 9 \times 5$ (third row) and $17 \times 17 \times 5$ (forth row) kernels; and final segmentation (fifth row) with color-coded ground truth edges, false positive errors, and false negative errors (red, yellow, and pink points, respectively). Only these two kernels were used in our experiments, because after the second smoothing the overall segmentation accuracy improves insignificantly.

III. EXPERIMENTAL RESULTS

The segmentation accuracy and robustness were evaluated on our own collection of 3D CT chest images for 30 subjects, abbreviated UoLDB below, and two publicly available sets from the ISBI 2012 VESsel SEgmentation in the Lung (VESSEL) challenge [35], [36] (20 subjects) and MICCAI 2011 LObe and Lung Analysis (LOLA11) challenge [37] (55 subjects). The images have been acquired with different scanners and data collection protocols and presented both normal lungs and various lung pathologies.

The 50 (20 training and 30 test) UoLDB images of size from $512 \times 512 \times 270$ to $512 \times 512 \times 450$ have been collected with a multi-detector GE Light Speed Plus scanner (General Electric, Milwaukee, USA) with the imaging protocols of 140 kV; 100 mA; slice thickness from 0.703 to 2.50 mm; scanning pitch 1.5, and field-of-view 36 cm. Fig. 4 details our 3D lung segmentation results for one subject from the UoLDB. Our segmentation employs only two GSS filtering stages because its overall accuracy improved insignificantly beyond the second stage in a few pilot experiments.

In order to highlight advantages of the integration of visual appearance descriptors with the adaptive shape descriptor, the test UoLDB images were also segmented by combining only the visual appearance descriptors, characterizing the original and GSS-filtered intensities and their pairwise co-occurrences.

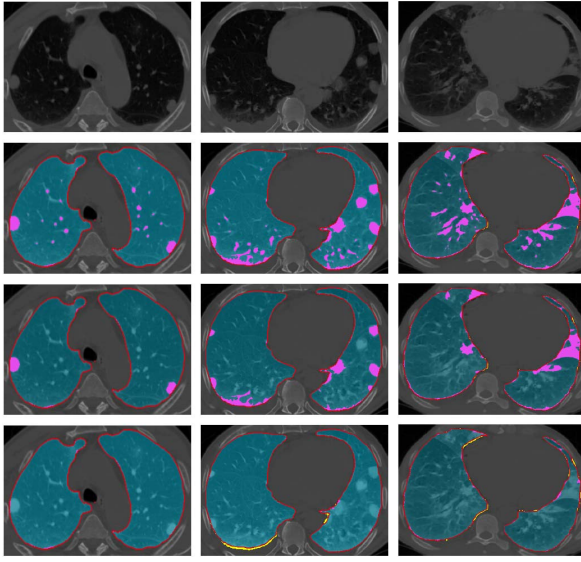


Fig. 5. Impacts of elements of our segmentation for three UoLDB subjects: original 2D chest sections (*first row*) and lung regions found for the original intensities and spatial interactions (*second row*); combined original/GSS-filtered intensities and spatial interactions (*third row*); and combined original/GSS-filtered intensities and spatial interactions, together with the adaptive shape model (*fourth row*). Same color ground truth and error coding as in [Fig. 4](#).

TABLE I

DSC, BHD, AND PVD ACCURACY (MEAN \pm STANDARD DEVIATION) OF DIFFERENT COMPONENTS (FEATURE GROUPS FG) OF OUR FRAMEWORK ON THE UoLDB IN TERMS OF THE:
FG1(INTENSITIES AND SPATIAL INTERACTIONS),
FG2 (COMBINED ORIGINAL / GSS-FILTERED
INTENSITIES AND SPATIAL INTERACTIONS),
FG3 (FG2 + ADAPTIVE SHAPE PRIORS)

UoLDB (30 test images)		
	DSC, %	BHD, mm
FG1	0.932 \pm 0.032	13.2 \pm 4.6
FG2	0.966 \pm 0.017	9.53 \pm 2.92
FG3	0.984 \pm 0.010	2.20 \pm 1.00
<i>p</i> -value	< 0.0001	< 0.0001
		< 0.0001

The resulting accuracy for three UoLDB subjects in [Fig. 5](#) was low—due to similar original voxel intensities, the pathological lung tissues were included into the segmented chest, rather than lungs. The segmentation error decreased after adding the GSS-filtered appearance descriptors and improved even further after integrating all the appearance descriptors with the adaptive shape prior. More results for subjects with different types of pathologies are shown in [Fig. 6](#).

The segmentation accuracy was evaluated for each test 3D CT image with the Dice similarity coefficient (DSC) [38], bidirectional Hausdorff distance (BHD), and percentage volume difference (PVD) [39], which characterize spatial overlaps, maximum surface-to-surface distances, and volume differences, respectively, between the segmented and “ground-truth” lung regions. [Table I](#) summarizes the DSC, BHD, and PVD statistics for all the test UoLDB data to show the effect of different feature groups (FG) of our framework. The ground-truth lung borders were outlined manually by a radiologist.

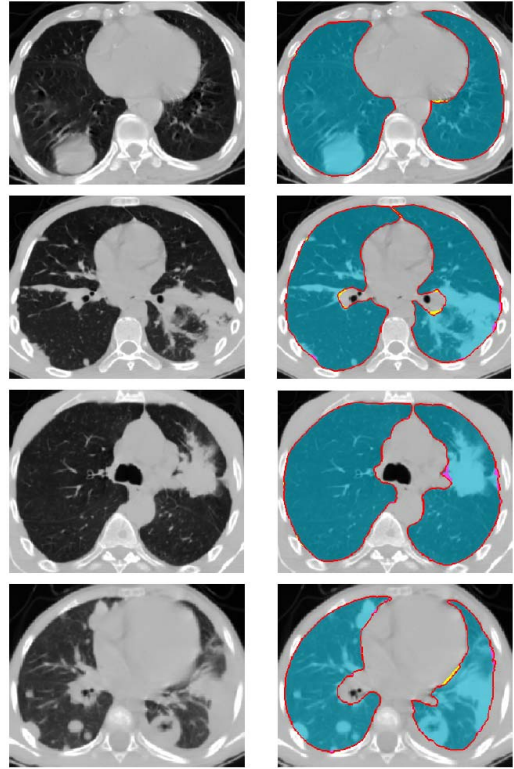


Fig. 6. Other four subjects from the UoLDB: original CT chest images with different pathologies: (left: *from top to bottom*) lung mass; consolidation; lung cancer, and cavitation + consolidation pathologies, and our segmentation (right: the same color ground truth and error coding as in [Fig. 4](#)).

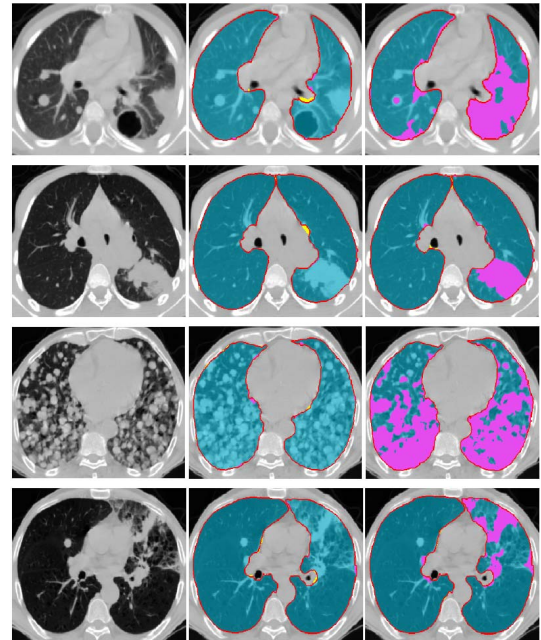


Fig. 7. Comparative segmentation of the UoLDB: *First row* – original CT sections with, *from top to bottom*, plural effusion and lung nodules; consolidation; pulmonary sarcoidosis, and fibrosis; *second row* – our segmentation, and *third row* – the FC segmentation [10] (the same color ground truth and error coding as in [Fig. 4](#)).

The accuracy of our pathological lungs segmentation method is also highlighted by comparing its performance against the traditional fuzzy connectedness (FC)-based lung

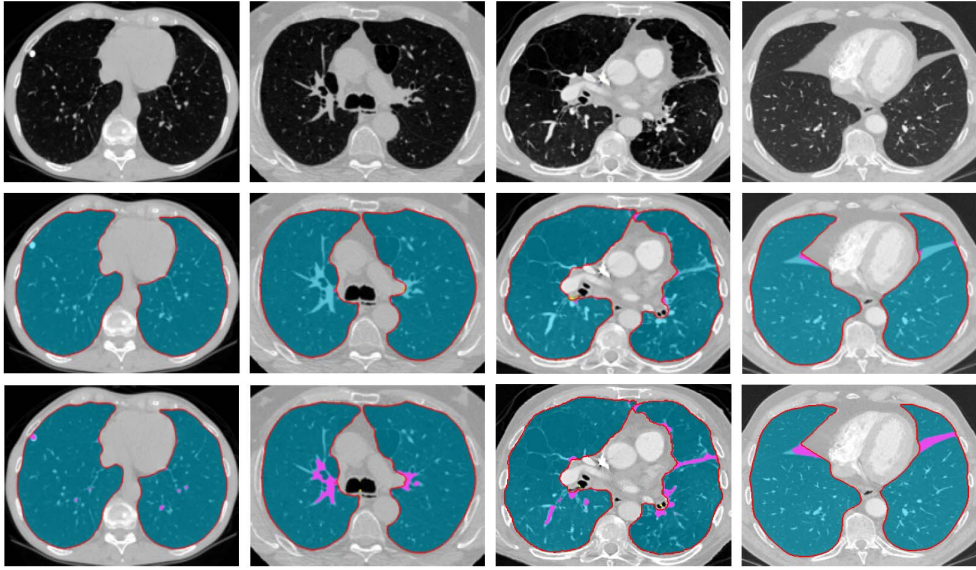


Fig. 8. Comparative segmentation of the VESSEL [35] database: original CT sections (*first row*); our segmentation (*second row*); and the FC segmentation (*third row*) [10] (the same color ground truth and error coding as in Fig. 4).

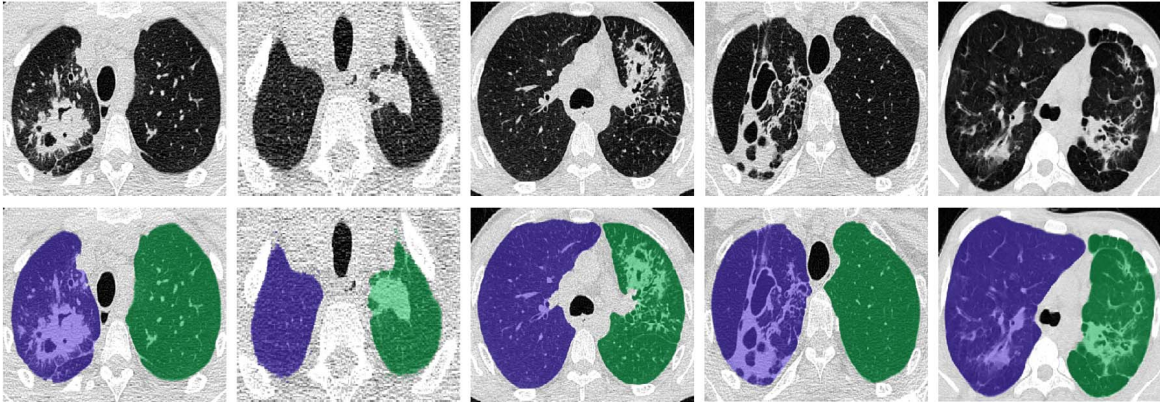


Fig. 9. Segmenting pathological lungs from the LOLA11 database. *First row* –Original CT sections with, from left to right, fibrosis, lung mass (tumor), consolidation, cavitation + fibrosis, and our segmentation is in the *second row* (its accuracy has been evaluated by the LOLA11 organizers [37]).

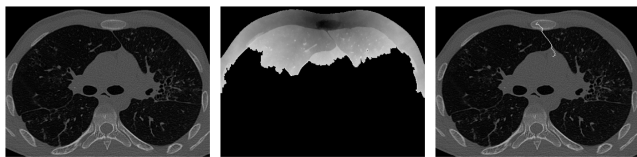


Fig. 10. Lung separation process; an original slice (*left*); generated energies of pixels traversed until finding the optimum path (*middle*), and the original image with the overlaid separating path (*right*).

segmentation [10], having a publicly available open-source software Lung Segmentation Tool (<http://www.nitrc.org/projects/nihlungseg/>). These experiments used the best performing manual seeding mode, recommended in its video tutorial default settings for refining segmented region maps: filling holes with a 3 mm-diameter binary filter and checking fuzzy connectedness. Fig. 7 compares our and FC segmentation qualitatively on a representative set of four pathological lungs from the UoLDB. The DSC, BHD, and PVD statistics for the UoLDB in Table II show that our segmentation, accounting for both short/long-range local and global lung properties, is

TABLE II
DSC, BHD, AND PVD ACCURACY (MEAN \pm STANDARD DEVIATION) OF OUR AND FC SEGMENTATION [10] ON THE UoLDB AND VESSEL [35] DATABASES

	UoLDB (30 test images)		
	DSC, %	BHD, mm	PVD, %
Our segm.	0.984 ± 0.010	2.20 ± 1.00	0.42 ± 0.10
FC [10]	0.906 ± 0.098	19.0 ± 9.9	15.4 ± 15.3
<i>p</i> -value	< 0.0001	< 0.0001	< 0.0001
	VESSEL [35] (20 test images)		
Our segm.	0.990 ± 0.005	2.10 ± 1.60	0.39 ± 0.20
FC [10]	0.967 ± 0.013	11.5 ± 5.1	2.40 ± 1.20
<i>p</i> -value	< 0.0001	< 0.0001	< 0.0001

more accurate. Differences between the metrics means for our and FC are statistically significant by the paired *t*-test (corresponding *p*-values are below 0.0001).

To evaluate its robustness to a chosen CT scanner and scanning protocol, our segmentation was tested against the FC framework on the VESSEL database [35] containing the

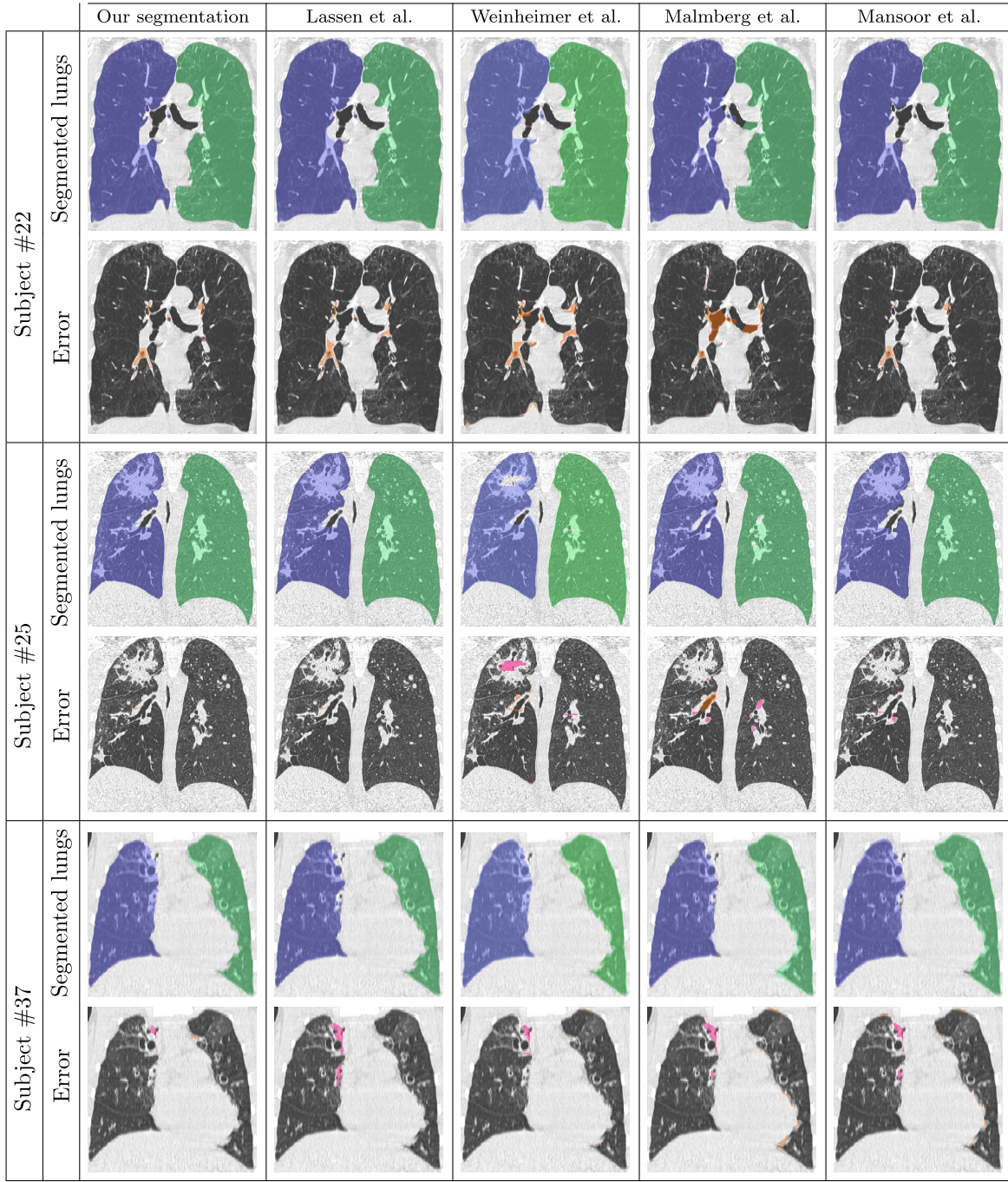


Fig. 11. Our segmentation for three subjects from the LOLA11 database vs. the 2nd- to 5th-rank LOLA11 competitors (the LOLA11 organizers [37] compared the extracted lungs with their ground truth and accounted for differences, being orange/pink-coded in the above region maps, to evaluate the overall accuracy).

CT chest images of mostly normal and a few pathological lungs. The VESSEL data sets were collected with different scanners and protocols. More details can be found in [36]. Fig. 8 qualitatively compares both frameworks, and the DSC, BHD, and PVD statistics for segmenting the whole VESSEL database are presented in Table II. The ground truth for this database was provided by the ISBI 2012 VESSEL challenge organizers.

Finally, our segmentation has been tested on the LOLA11 database [37], acquired by different scanners and protocols for 55 subjects with diverse lung pathologies. To follow the

LOLA11 challenge regulations, the trachea and main bronchi have been removed from the LOLA11 image by customized region growing, which terminates after the trachea starts to split into four components. Then, if necessary, the lungs were separated with the optimal path finder [40] searching for intensity differences. The search is conducted on a 2D axial slice after finding a single connected component with a lung volume being nearly equal to the volume of the lung components in the previous slice. The finder connects two automatically initialized points in the chest region that separates the left and right lungs, as described in [40]. Fig. 10 shows an example

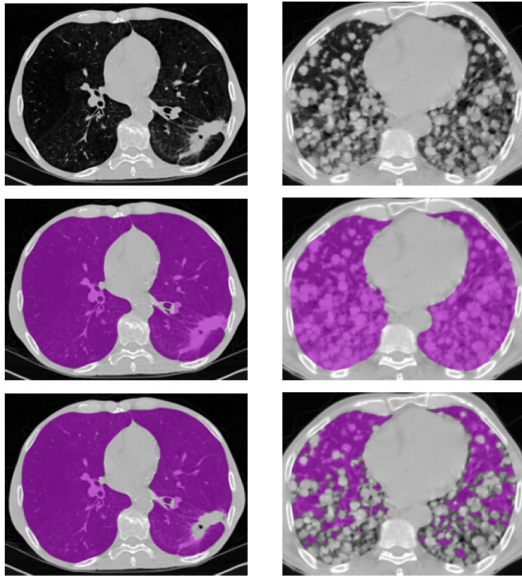


Fig. 12. Total accuracy reduction due to erroneous segmentation of pathological tissues (*first row*) between ground truth (*second row*) and pathological-missing segmentation (*third row*): only 0.1% for missing the lung mass for a tumor (*left column*), but about 30% for a severe pathology (*right column*).

slice together with its calculated pixel-wise energies to search for the optimum path between the two automatically initialized points and the separation path found.

The LOLA11 challenge organizers blindly compared our results, exemplified in Fig. 9, to the ground truth and reported the mean right and left lungs overlaps over all the 55 scans. Table III and Fig. 11 compare the top-rank LOLA11 methods, our results having the first rank out of the 16 competitors.

IV. CONCLUSIONS

Accurate segmentation of lung images, especially in the case of pathological lungs with, e.g., lung nodules, is essential for reliable CAD of pulmonary and lung diseases. Most segmentation errors are due to missing pathological tissues; however, these errors negligibly affect the overall segmentation accuracy because the pathological tissue volume is often very small compared to the whole lung volume, as in Fig. 12(left column). Nonetheless, segmentation inaccuracies of these types of tumors are a serious problem, because the undetected and non-localized tumor candidates will compromise the further analysis, e.g., detection and diagnostics, in any CAD system and preclude the early cancer diagnosis of a patient. Even though missing the tumor in Fig. 12(left column) reduces the overall DSC by only 0.1%, it may explain the small difference (0.7%) between the mean overlap scores for our segmentation and the closest competitor on the LOLA11 challenge database of pathological lungs. Moreover, if a severe lung pathology affects a larger portion of the total lung volume, the inaccurate segmentation of these tissues will considerably reduce the overall accuracy, such as in Fig. 12(right column) where the overall DSC has decreased by 30.4%. Therefore, accurate lung segmentation for various pathologies is a must for choosing a proper region of interest for subsequent CAD steps.

The methodology proposed in this paper can accurately segment a wide range of pathological lungs from the 3D

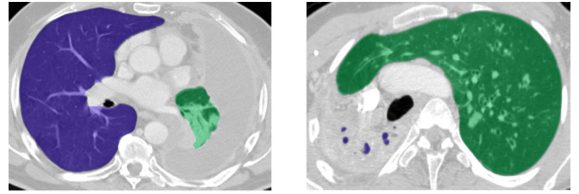


Fig. 13. Impacts of severe right and left lung pathologies on our segmentation accuracy: the ground-truth-to-left-lung overlaps of 87.4% (*left*) and 5.2% (*right*), the true lung maps being available to only the LOLA11 organizers.

TABLE III

MEAN \pm STANDARD DEVIATION OVERLAP OF OUR SEGMENTATION WITH THE GROUND TRUTH FOR THE ENTIRE LOLA11 DATABASE OF 55 CHEST CT IMAGES VS. THE 2ND–5TH-RANK LOLA11 COMPETITORS (THESE ACCURACIES WERE PROVIDED BY THE LOLA11 ORGANIZERS [37])

Segmentation Method				
Our	[41]	[42]	[43]	[10]
0.980 \pm 0.075	0.973 \pm 0.116	0.970 \pm 0.113	0.969 \pm 0.134	0.968 \pm 0.116

chest CT scans due to the combining first- and second-order probabilistic descriptors of the original and GSS-smoothed images with the proposed appearance-guided adaptive shape prior. The latter requires a reasonably large training set of healthy and pathological lungs. To be accurately aligned, both the right and left lungs in each input CT image should have some healthy tissues to be used as guiding landmarks for alignment. Therefore, too small healthy sections in either the left or right lung will affect our segmentation performance, as demonstrated in Fig. 13. To extend the scope of the proposed segmentation technique in the future, we plan to append the healthy tissues with other chest landmarks.

The high DSC, MHD, and PVD accuracy of our lung segmentation framework has been confirmed experimentally on multiple *in-vivo* 3D CT image datasets. What is most importantly, the blind comparison with the publicly-available LOLA11 database has validated the superior performance of our framework over many existing methods in segmenting various pathological lung images, ranging from mild to severe cases, such as pulmonary fibrosis, pleural effusion, consolidation, and cavities. These wider capabilities stem from using the adaptive prior shape model of the lungs to derive more accurate visual appearance descriptions of the chest CT images. The resulting higher accuracy can be beneficial for any current CAD system that uses lung segmentation as a critical initial step for measuring or estimating various biomarkers, such as a whole lung volume, left and right lungs volumes, and so forth [44]. These biomarkers assist in diagnosing many restrictive / obstructive lung diseases, such as interstitial lung disease, chronic obstructive pulmonary disease, extrinsic disorders, and asthma. Finally, our framework can enhance the accuracy of any lung CAD system, e.g., the one for early detection of lung nodules because the correctly extracted lung fields constrain and accurately identify nodules' search space.

APPENDIX I LIST OF ALGORITHMS

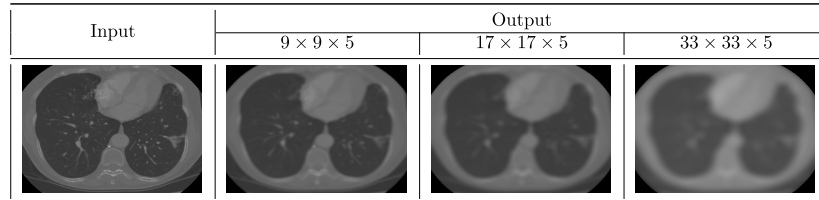


Fig. 14. Axial planar sections of the original 3D CT image and its GSS-smoothed versions obtained with the $9 \times 9 \times 5$, $17 \times 17 \times 5$, and $33 \times 33 \times 5$ kernels.

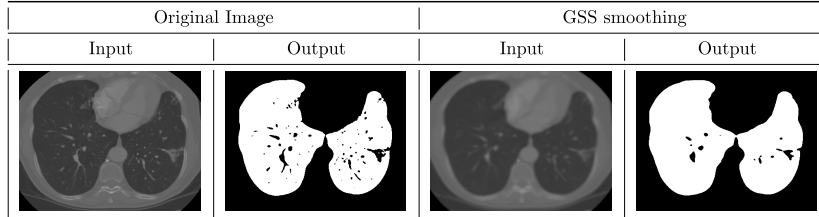


Fig. 15. Initial segmentation maps after voxel-wise classification by the LCDG modeling of original and GSS-smoothed images.

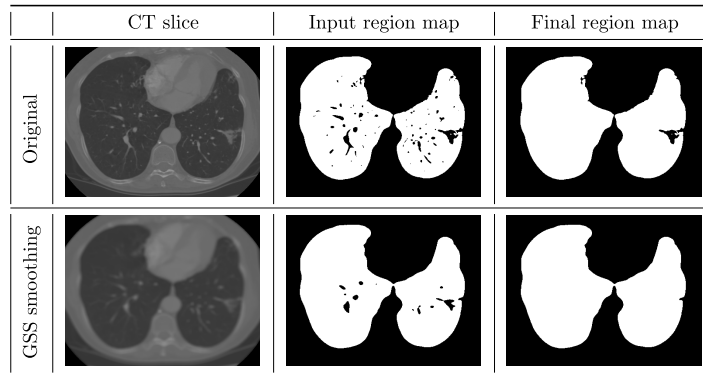


Fig. 16. MGRF-guided segmentation of original image and its GSS smoothed version.

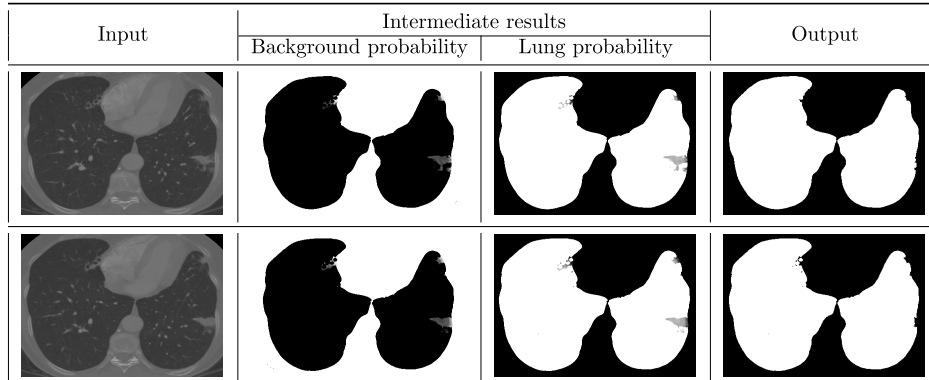


Fig. 17. Axial planar sections of the 3D CT images; background / lung shape probabilities, and the final segmentation maps.

Input: 3D-CT chest volume \mathbf{g}
Output: GSS-smoothed volumes $\mathbf{g}_\sigma = \mathbf{g} * \mathbf{h}_\sigma$; $\sigma^2 \in [4.5, 8.5]$

```

1 begin
2   | forall the  $\sigma^2 \in [4.5, 8.5]$  do
3   |   | // Generate the Gaussian kernel
4   |   |  $\mathbf{h}_\sigma = \left( h_{\sigma;\rho} = \frac{1}{(2\pi)^{1.5}\sigma^3} \exp\left(-\frac{1}{2\sigma^2}(x_\rho^2 + y_\rho^2 + z_\rho^2)\right) : \rho = (x_\rho, y_\rho, z_\rho) \in \mathbf{R}_{\text{kernel}} \right)$ 
5   |   | // Convolve the generated kernel with the input volume  $\mathbf{g}$ .
6   |   |  $\mathbf{g}_\sigma = \mathbf{g} * \mathbf{h}_\sigma = \left( g_{\sigma;\mathbf{r}} = \sum_{\rho \in \mathbf{R}_{\text{kernel}}} h_{\sigma;\rho} \cdot g_{\mathbf{r}-\rho} : \mathbf{r} \in \mathbf{R} \right)$ 
7   |   return  $\mathbf{g}_\sigma$ 
8 end
9 end

```

Fig. 18. Gaussian scale space smoothing, illustration is shown in Fig. 14.

Input: 3D-CT chest volume \mathbf{g}
Output: Initial segmentation map \mathbf{m}

```

1 begin
2   Collect the empirical gray level distribution  $\mathbf{F} = (F_q : q \in \mathbf{Q})$  for the input volume  $\mathbf{g}$ .
3   Approximate  $\mathbf{F}$  with a mixture  $\mathbf{P}_2 = w_0\mathbf{D}_0 + w_1\mathbf{D}_1$  of two DGs  $\mathbf{D}_k$ ;  $k \in \{0, 1\}$ ;  $w_0 + w_1 = 1$ , for two dominant modes
   of  $\mathbf{F}$  associated with background ( $k = 0$ ) and lung ( $k = 1$ ) voxels;  $\mathbf{P}_2 = (P_{2,q} : q \in \mathbf{Q})$ .
4   Approximate deviations,  $\Delta = (F_q - P_{2,q} : q \in \mathbf{Q})$ , between  $\mathbf{F}$  and  $\mathbf{P}_2$  with sign-alternate subordinate DGs:
5     Separate positive,  $\Delta_p = (\max\{\Delta_q, 0\} : q \in \mathbf{Q})$ , and negative,  $\Delta_n = (\min\{\Delta_q, 0\} : q \in \mathbf{Q})$ , deviations.
6     Form two scaled-up "distributions"  $\mathbf{F}_p = \frac{1}{s}\Delta_p$  and  $\mathbf{F}_n = -\frac{1}{s}\Delta_p$ ;  $s = \sum_{q \in \mathbf{Q}} \Delta_{p,q} \equiv -\sum_{q \in \mathbf{Q}} \Delta_{n,q}$ .
7     Approximate  $\mathbf{F}_p$  and  $\mathbf{F}_n$  with subordinate DG mixtures of estimated sizes  $C_p$  and  $C_n$ , respectively:
8        $\mathbf{P}_{p:C_p} = s \sum_{k=1}^{C_p} w_{p,k} \mathbf{D}_{n:k}$  and  $\mathbf{P}_{n:C_n} = s \sum_{l=1}^{C_n} w_{n,l} \mathbf{D}_{n:l}$ .
9     Add the scaled-down subordinate LCDG  $s(\mathbf{P}_{p:C_p} - \mathbf{P}_{n:C_n})$  to the mixture  $\mathbf{P}_2$  to get the initial LCDG:
10     $\mathbf{P}_C = w_0\mathbf{D}_0 + w_1\mathbf{D}_1 + s \sum_{k=1}^{C_p} w_{p,k} \mathbf{D}_{n:k} - s \sum_{l=1}^{C_n} w_{n,l} \mathbf{D}_{n:l}$  of size  $C = 2 + C_p + C_n$ .
11    // The initial LCDG has 2 positive weights  $w_0$  and  $w_1$  of the dominant DGs and  $C_p + C_n$  weights
12    // of the subordinate sign alternate DGs, such that  $\sum_{k=1}^{C_p} w_{p,k} - \sum_{l=1}^{C_n} w_{n,l} = 0$ .
13    Allocate the subordinate DGs to the lung or background dominant DG to minimize overlaps between the final separate
   lung and background LCDG models.
14 end

```

Fig. 19. 1st-order intensity modeling with linear combinations of discrete Gaussians (LCDG), illustration is shown in Fig. 15.

Input: Initial segmentation 3D map \mathbf{m} ; numbers of neighbors $c_{hvdc} = 8$, $c_{hvdu} = c_{hvdl} = 9$.
Output: 4D array $\mathbf{P} = (P_r[k] : r \in \mathbf{R}; k \in \{0, 1\})$.

```

1 begin
2   Read the initial 3D map  $\mathbf{m}$ 
3     // Calculate Gibbs potentials  $V_{a: eq}$  and  $V_{a: ne}$ ;  $a \in \{hvdc, hvdu, hvdl\}$  of Eq. (8) for the map  $\mathbf{m}$  by collecting
     frequencies  $f_{eq:a}(\mathbf{m})$  and  $f_{ne:a}(\mathbf{m}) = 1 - f_{eq:a}(\mathbf{m})$  of equal and non-equal neighboring pairs of region labels.
4   foreach neighborhood  $a \in \{hvdc, hvdu, hvdl\}$  do
5     |  $N_{eq:a} \leftarrow 0$ ;  $N_a \leftarrow 0$ 
6   end
7   foreach voxel  $r \in \mathbf{R}$  do
8     | foreach neighborhood  $a \in \{hvdc, hvdu, hvdl\}$  do
9       |   // Find the number  $v_{eq:a}$  of labels in the neighborhood  $a$ , which are equal to the label  $m_r$ .
10      |    $N_{eq:a} \leftarrow N_{eq:a} + v_{eq:a}$ ;  $N_a \leftarrow N_a + c_a$ 
11    end
12  end
13  // Calculate frequencies  $f_{eq:a}$  and negated potentials  $V_{eq:a}$  of equal labels.
14  foreach neighborhood  $a \in \{hvdc, hvdu, hvdl\}$  do
15    |  $f_{eq:a} \leftarrow \frac{N_{eq:a}}{N_a}$ ;  $V_{eq:a} \leftarrow 4f_{eq:a} - 2$ ;  $V_{ne:a} = -V_{eq:a}$ 
16  end
17  // Compute transitional probabilities  $\mathbf{P}$  using voxel-wise Gibbs neg-energies  $E[k]$ 
18  foreach voxel  $r \in \mathbf{R}$  do
19    | foreach label  $k$  do
20      |   // Compute the voxel-wise neg-energies  $E_0$  and  $E_1$ .
21      |    $E_k \leftarrow 0$ 
22      |   foreach neighborhood  $a \in \{hvdc, hvdu, hvdl\}$  do
23        |     // Find the number  $v_{eq:a:k}$  of neighboring voxel labels equal to  $k$ .
24        |      $E_k \leftarrow E_k + v_{eq:a:k} \cdot V_{eq:a} + (c_a - v_{eq:a:k}) \cdot V_{ne:a}$ 
25      end
26    end
27    foreach label  $k$  do
28      |  $P_r[k] = \frac{\exp(E_k)}{\exp(E_0) + \exp(E_1)}$ 
29    end
30  end
31  return  $\mathbf{P}$ 
32 end

```

Fig. 20. Learning the MGRF model of the input map, illustration is shown in Fig. 16.

Input: Test image \mathbf{t} ; co-aligned training database $B = \{\mathbf{g}_i : i = 1, \dots, N\}$.
Output: 4D shape prior $\mathbf{P}_{sh} = (P_{sh:r} : r \in \mathbf{R})$

```

1 begin
2   // Align  $\mathbf{t}$  to  $B$  and store the deformation field  $\psi$  that maps each test voxel to the database domain
3   // Select top  $J$  database images by normalized cross correlation (NCC) with the co-aligned test image
4   foreach image  $g_i \in B$  do
5      $NCC_{t,g_i} = \frac{\sum_{r \in R} (t_r - \mu_t)(g_{i,r} - \mu_{g_i})}{\sqrt{\sum_{r \in R} (t_r - \mu_t)^2} \sqrt{\sum_{r \in R} (g_{i,r} - \mu_{g_i})^2}}$ 
6   end
7   // Form the atlas  $B_A$  from  $J$  closest, by the NCC, training images.
8   foreach voxel  $r \in \mathbf{R}$  do
9     // Map the voxel  $r$  to the atlas  $B_A$  using the deformation field  $\psi$ .
10    while matches between the signal  $t_r$  and the atlas signals are not found do
11      // Initialize the matching tolerance:  $\tau \leftarrow \tau_{init}$ 
12      // Loop until  $\tau$  reaches a predefined threshold  $\xi$ 
13      while  $\tau < \xi$  do
14        // Find within the search cube  $C_{r:\alpha}$  a subset of all matching voxels  $v_r = \bigcup_{j=1}^J v_{j:r}$  where
15         $v_{j:r} = \{\rho : \rho \in C_r; |t_r - g_{j:\rho}| \leq \tau\}$  is the matching subset in the atlas image  $g_j \in B_A$ .
16        if matching voxels are found in  $C_r$  then
17          // Compute the voxel-wise region label probability  $P_{sh:r}(k)$ ;  $k \in \{0, 1\}$ , using the training labels and
18          // the numbers of voxels  $v_{j:r}$  in the subsets  $v_{j:r}$ .
19           $v_r \leftarrow \sum_{j=1}^J v_{j:r}$ 
20           $P_{sh:r}(k) \leftarrow \frac{1}{v_r} \sum_{j=1}^J \sum_{\rho \in v_{j:r}} \delta(k - m_{j:\rho})$ ;  $k \in \{0, 1\}$ 
21          // where  $\delta(w)$  is the Kronecker's delta-function:  $\delta(0) = 1$  and  $\delta(w) = 0$  for  $w \neq 0$ .
22          break
23        else
24          // increment the matching threshold
25           $\tau \leftarrow \tau + \Delta_\tau$ 
26        end
27      end
28      // increment the search cube size
29       $\alpha \leftarrow \alpha + \Delta_{size}$ 
30    end
31  end
32  return  $\mathbf{P}_{sh}$ 
33 end

```

Fig. 21. Adaptive shape prior, illustration is shown in Fig. 17.

REFERENCES

- [1] A. Cunliffe, S. G. Armato, R. Castillo, N. Pham, T. Guerrero, and H. A. Al-Hallaq, "Lung texture in serial thoracic computed tomography scans: Correlation of radiomics-based features with radiation therapy dose and radiation pneumonitis development," *Int. J. Rad. Oncol. Biol. Phys.*, vol. 91, no. 5, pp. 1048–1056, 2015.
- [2] S. G. Armato and W. F. Sensakovic, "Automated lung segmentation for thoracic CT: Impact on computer-aided diagnosis," *Acad. Radiol.*, vol. 11, no. 9, pp. 1011–1021, 2004.
- [3] S. Hu, E. Hoffman, and J. Reinhardt, "Automatic lung segmentation for accurate quantitation of volumetric X-ray CT images," *IEEE Trans. Med. Imag.*, vol. 20, no. 6, pp. 490–498, Jun. 2001.
- [4] A. M. Mendonca, J. A. D. Silva, and A. Campilho, "Automatic delimitation of lung fields on chest radiographs," in *Proc. IEEE Int. Symp. Biomed. Imag.*, vol. 2, Apr. 2004, pp. 1287–1290.
- [5] P. Campadelli, E. Casiraghi, and D. Artioli, "A fully automated method for lung nodule detection from postero-anterior chest radiographs," *IEEE Trans. Med. Imag.*, vol. 25, no. 12, pp. 1588–1603, Dec. 2006.
- [6] B. van Ginneken, M. B. Stegmann, and M. Loog, "Segmentation of anatomical structures in chest radiographs using supervised methods: A comparative study on a public database," *Med. Image Anal.*, vol. 10, no. 1, pp. 19–40, 2006.
- [7] P. Korfiatis, S. Skiadopoulos, P. Sakellaropoulos, C. Kalogeropoulou, and L. Costaridou, "Combining 2D wavelet edge highlighting and 3D thresholding for lung segmentation in thin-slice CT," *Brit. J. Radiol.*, vol. 80, no. 960, pp. 996–1004, 2007.
- [8] M. Silveira, J. Nascimento, and J. Marques, "Automatic segmentation of the lungs using robust level sets," in *Proc. IEEE Int. Conf. Eng. Med. Biol.*, Aug. 2007, pp. 4414–4417.
- [9] J. C. Ross *et al.*, "Lung extraction, lobe segmentation and hierarchical region assessment for quantitative analysis on high resolution computed tomography images," in *Proc. Med. Image Comput. Comput.-Assisted Intervent.*, vol. 5762, 2009, pp. 690–698.
- [10] A. Mansoor *et al.*, "A generic approach to pathological lung segmentation," *IEEE Trans. Med. Imag.*, vol. 33, no. 12, pp. 2293–2310, Dec. 2014.
- [11] J. Wang, F. Li, and Q. Li, "Automated segmentation of lungs with severe interstitial lung disease in CT," *Med. Phys.*, vol. 36, no. 10, pp. 4592–4599, 2009.
- [12] T. Kockelkorn *et al.*, "Interactive lung segmentation in abnormal human and animal chest CT scans," *Med. Phys.*, vol. 41, no. 8, p. 081915, 2014.
- [13] J. Zhou, B. Zhang, G. Lasio, K. Prado, and W. D'Souza, "SU-F-BRF-02: Automated lung segmentation method using atlas-based sparse shape composition with a shape constrained deformable model," *Med. Phys.*, vol. 41, no. 6, p. 399, 2014.

- [14] I. Sluimer, M. Prokop, and B. Van Ginneken, "Toward automated segmentation of the pathological lung in CT," *IEEE Trans. Med. Imag.*, vol. 24, no. 8, pp. 1025–1038, Aug. 2005.
- [15] S. Sun, C. Bauer, and R. Beichel, "Automated 3-D segmentation of lungs with lung cancer in CT data using a novel robust active shape model approach," *IEEE Trans. Med. Imag.*, vol. 31, no. 2, pp. 449–460, Feb. 2012.
- [16] E. M. van Rikxoort, B. de Hoop, M. A. Viergever, M. Prokop, and B. van Ginneken, "Automatic lung segmentation from thoracic computed tomography scans using a hybrid approach with error detection," *Med. Phys.*, vol. 36, pp. 2934–2947, 2009.
- [17] K. Nakagomi, A. Shimizu, H. Kobatake, M. Yakami, K. Fujimoto, and K. Togashi, "Multi-shape graph cuts with neighbor prior constraints and its application to lung segmentation from a chest CT volume," *Med. Image Anal.*, vol. 17, no. 1, pp. 62–77, 2013.
- [18] P. Korfiatis, C. Kalogeropoulou, A. Karahaliou, A. Kazantzi, S. Skiadopoulos, and L. Costaridou, "Texture classification-based segmentation of lung affected by interstitial pneumonia in high-resolution CT," *Med. Phys.*, vol. 35, no. 12, pp. 5290–5302, 2008.
- [19] B. Lassen, J.-M. Kuhnigk, O. Friman, S. Krass, and H.-O. Peitgen, "Automatic segmentation of lung lobes in ct images based on fissures, vessels, and bronchi," in *Proc. IEEE Int. Symp. Biomed. Imag.*, Apr. 2010, pp. 560–563.
- [20] N. Birkbeck *et al.*, "Lung segmentation from CT with severe pathologies using anatomical constraints," in *Proc. Med. Image Comput. Comput.-Assisted Intervent.*, 2014, vol. 8673, no. 1, pp. 804–811.
- [21] T. Kockelkorn, E. M. van Rikxoort, J. C. Grutters, and B. van Ginneken, "Interactive lung segmentation in CT scans with severe abnormalities," in *Proc. IEEE Int. Symp. Biomed. Imag.*, Apr. 2010, pp. 564–567.
- [22] P. Hua, Q. Song, M. Sonka, E. A. Hoffman, and J. M. Reinhardt, "Segmentation of pathological and diseased lung tissue in CT images using a graph-search algorithm," in *Proc. IEEE Int. Symp. Biomed. Imag.*, Mar./Apr. 2011, pp. 2072–2075.
- [23] A. El-Baz *et al.*, "Computer-aided diagnosis systems for lung cancer: Challenges and methodologies," *Int. J. Biomed. Imag.*, vol. 2013, 2013, Art. no. 942353.
- [24] K. Li, X. Wu, D. Z. Chen, and M. Sonka, "Optimal surface segmentation in volumetric images—A graph-theoretic approach," *IEEE Trans. Pattern Anal. Mach. Intell.*, vol. 28, no. 1, pp. 119–134, Jan. 2006.
- [25] M. Sofka *et al.*, "Multi-stage learning for robust lung segmentation in challenging CT volumes," in *Proc. Med. Image Comput. Comput.-Assisted Intervent.*, 2011, pp. 667–674.
- [26] J. K. Udupa and S. Samarasekera, "Fuzzy connectedness and object definition: Theory, algorithms and applications in image segmentation," *Graph. Models Image Process.*, vol. 58, no. 3, pp. 246–261, 1996.
- [27] B. Glocker, A. Sotiras, N. Komodakis, and N. Paragios, "Deformable medical image registration: Setting the state of the art with discrete methods," *Ann. Rev. Biomed. Eng.*, vol. 13, pp. 219–244, Aug. 2011.
- [28] T. Lindeberg, "Generalized Gaussian scale-space axiomatics comprising linear scale-space, affine scale-space and spatio-temporal scale-space," *J. Math. Imag. Vis.*, vol. 40, no. 1, pp. 36–81, 2011.
- [29] A. A. Farag, A. S. El-Baz, and G. Gimel'farb, "Precise segmentation of multimodal images," *IEEE Trans. Image Process.*, vol. 15, no. 4, pp. 952–968, Apr. 2006.
- [30] G. L. Gimel'farb, *Image Textures and Gibbs Random Fields*. Norwell, MA, USA: Kluwer, 1999.
- [31] B. Glocker, N. Komodakis, G. Tziritas, N. Navab, and N. Paragios, "Dense image registration through MRFs and efficient linear programming," *Med. Image Anal.*, vol. 12, no. 6, pp. 731–741, 2008.
- [32] B. Glocker, N. Komodakis, N. Paragios, and N. Navab, "Non-rigid registration using discrete MRFs: Application to thoracic CT images," in *Proc. Med. Image Anal. Clinic Grand Challenge*, 2010, pp. 147–154.
- [33] Y. Lu, I. Cohen, X. S. Zhou, and Q. Tian, "Feature selection using principal feature analysis," in *Proc. 15th ACM Int. Conf. Multimedia*, 2007, pp. 301–304.
- [34] A. El-Baz *et al.*, "Precise segmentation of 3-D magnetic resonance angiography," *IEEE Trans. Biomed. Eng.*, vol. 59, no. 7, pp. 2019–2029, Jul. 2012.
- [35] (2012). *VEssel SEgmentation in the Lung 2012*. [Online]. Available: <http://vessel12.grand-challenge.org/>
- [36] R. D. Rudyanto *et al.*, "Comparing algorithms for automated vessel segmentation in computed tomography scans of the lung: The VESSEL12 study," *Med. Image Anal.*, vol. 18, no. 7, pp. 1217–1232, 2014.
- [37] (2011). *LObe and Lung Analysis 2011*. [Online]. Available: <http://lolal11.com/>
- [38] K. H. Zou *et al.*, "Statistical validation of image segmentation quality based on a spatial overlap index," *Acad. Radiol.*, vol. 11, no. 2, pp. 178–189, Feb. 2004.
- [39] G. Gerig, M. Jomier, and M. Chakos, "Valmet: A new validation tool for assessing and improving 3D object segmentation," in *Proc. Med. Image Comput. Comput.-Assisted Intervent.*, Utrecht, The Netherlands, Oct. 2001, pp. 516–523.
- [40] M. S. Brown *et al.*, "Method for segmenting chest CT image data using an anatomical model: Preliminary results," *IEEE Trans. Med. Imag.*, vol. 16, no. 6, pp. 828–839, Dec. 1997.
- [41] B. Lassen, E. M. van Rikxoort, M. Schmidt, S. Kerkstra, B. van Ginneken, and J.-M. Kuhnigk, "Automatic segmentation of the pulmonary lobes from chest CT scans based on fissures, vessels and bronchi," *IEEE Trans. Med. Imag.*, vol. 32, no. 2, pp. 210–222, Feb. 2013.
- [42] O. Weinheimer, T. Achenbach, C. P. Heussel, and C. Düber, "Automatic lung segmentation in MDCT images," in *Proc. 4th Int. Workshop Pulmonary Image Anal.*, Toronto, ON, Canada, 2011, pp. 241–255.
- [43] F. Malmberg, R. Nordenskjöld, R. Strand, and J. Kullberg, "Smartpaint: A tool for interactive segmentation of medical volume images," in *Proc. Comput. Methods Biomech. Biomed. Eng., Imag. Vis.*, 2014, pp. 1–9.
- [44] A. Fernandez-Bustamante *et al.*, "Early effect of tidal vol. on, lung injury biomarkers in surgical patients with healthy lungs," *Anesthesiology*, vol. 121, no. 3, pp. 469–481, 2014.